Non-Native Aggregation of α-Chymotrypsinogen Occurs through Nucleation and Growth with Competing Nucleus Sizes and Negative Activation Energies†

Jennifer M. Andrews and Christopher J. Roberts*

Department of Chemical Engineering, University of Delaware, Newark, Delaware 19716

Received February 12, 2007; Revised Manuscript Received April 11, 2007

ABSTRACT: The kinetics and structural transitions of non-native aggregation of α-chymotrypsinogen (aCgn) were investigated over a wide range of temperature and initial protein concentration at pH 3.5, where high molecular weight aggregates remained soluble throughout the reaction. A comparison of thermodynamic, kinetic, and spectroscopic data shows that aggregation under non-native-favoring conditions proceeds through a molten globule unfolded monomer state, with a nucleation and growth mechanism. Formation of irreversible aggregates and conversion to β-sheet secondary structures occur simultaneously without detectable intermediates, suggesting that β-sheet formation may be a commitment step during the nucleation and growth stages. Analysis of the kinetics using a Lumry−Eyring with nucleated polymerization (LENP) model provides the predominant nucleus size and the product of the intrinsic nucleation and intrinsic growth time scales at each state point. We find that the nucleus size depends on both temperature and protein concentration, and in some cases there is competition between two distinct nucleus sizes. The observed rate coefficient (k_{obs}) for aggregation displays a maximum as a function of temperature because of the competition between folding−unfolding thermodynamics and the intrinsic growth and nucleation rates; the latter contribution has a large, negative activation enthalpy that dominates k_{obs} at elevated temperatures. Temperature-jump experiments reveal that aggregates depolymerize at high temperatures, indicating that they are lower in enthalpy than the free monomer. Overall, the results suggest more generally that non-native aggregation may proceed through more than one nucleus size and that intrinsic kinetics of nucleation and growth may have significant entropic barriers.

Non-native protein and polypeptide aggregation generally refers to the process by which initially native or unfolded proteins or polypeptides spontaneously self-assemble to form relatively high molecular weight (MW[1]) aggregates composed of individual monomers that have adopted significantly non-native secondary structures; the prevalent aggregate secondary structure often being β-sheet (*1*−*7*). In many cases the resulting aggregates occur as soluble or insoluble filaments, fibrils, or flocculated or gelled polymers (*8*−*10*).

Non-native aggregation poses significant problems for the biopharmaceutical industry, resulting in loss of viable product and in potential safety concerns during both production and storage (*1*, *11*−*16*). Aggregation has also been linked to a number of debilitating ailments such as Alzheimer's, Parkinson's, Huntington's, and prion-based diseases (*1*, *2*, *8*, *17*, *18*). An improved ability to discern details of the underlying mechanism (*19*−*23*) as well as predict the resulting kinetics (*24*−*27*) would potentially aid identification of more effective treatments for such diseases as well as more effective stabilization strategies for biopharmaceutical products.

The present work is concerned with the net irreversible, non-native assembly of α-chymotrypsinogen A (aCgn), resulting in soluble, relatively high MW aggregates such as those commonly observed *in vitro* under mildly acidic or weakly denaturing conditions for a variety of pharmaceutically and medically relevant proteins and polypeptides (*1*, *10*, *28*, *29*). aCgn was selected as a well-characterized, natively monomeric, globular protein with relatively simple unfolding thermodynamics and kinetics that forms non-native aggregates on reasonable time scales at elevated temperatures (*30*, *31*).

The majority of the results presented in this article were obtained under non-native favoring conditions (elevated temperatures) at pH 3.5 and low ionic strength. At these solution conditions, the aggregates remain soluble and the native, unfolded, and aggregate states have distinguishable secondary and tertiary structures. These features allow for direct spectroscopic characterization and monitoring of both (un)folding and aggregate formation. The non-native monomer of aCgn is not fully unfolded under these conditions (*31*) and is capable of reversible unfolding *in vitro*. It is known from work elsewhere in our laboratory that at these solution conditions aCgn has net repulsive interactions between monomers (positive second osmotic virial coef-

† This work was supported in part by the University of Delaware Research Foundation, Boehringer Ingelheim Pharmaceuticals, and by NIH Grant No. P20 RR-015588 from the National Center for Research Resources.

* To whom correspondence should be addressed. Tel: 302-831-0838. E-mail: cjr@udel.edu.

[1] Abbreviations: aCgn, α-chymotrypsinogen A; COM, spectral center of mass; LENP, Lumry−Eyring with nucleated polymerization; *MG*, molten globule monomer; MRE, mean residue ellipticity; MW, molecular weight; $\langle MW \rangle_w$, weight-averaged molecular weight; *m*, mass fraction monomer remaining; *N*, native monomer; *U*, unfolded monomer; *R*, aggregation-prone monomer conformational state; SEC, size-exclusion chromatography; SLS, static light scattering.

10.1021/bi700296f CCC: $37.00
Published on Web 05/27/2007

Scheme 1: Lumry−Eyring Nucleated Polymerization or Extended Lumry−Eyring Scheme for Non-Native Protein Aggregation (Adapted from Ref *36*)

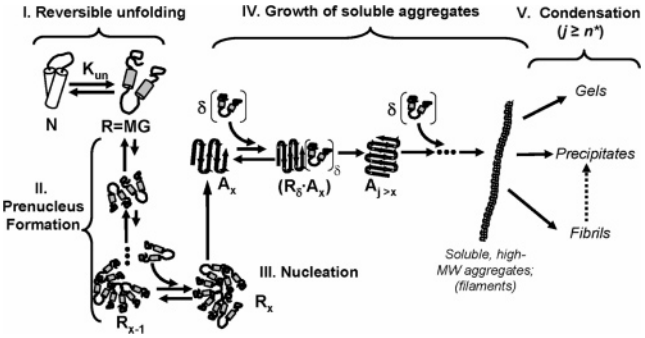

ficient) and that the soluble aggregates formed are essentially linear, high MW polymers of aCgn monomers (Weiss, W. F., IV, unpublished work). Using the approach and considerations outlined below, we sought to gain insights into the mechanism of aCgn aggregation. Furthermore, we employ aCgn as a model system to develop a general approach for the study of non-native aggregation kinetics that quantitatively combines biophysical characterization and kinetic modeling. In what follows, we briefly review some salient aspects of non-native aggregation and the resulting kinetics that help motivate the experimental approach adopted here. The points outlined below also provide context for much of the results and discussion in later sections.

For proteins that are able to fold *in vitro*, Scheme 1 schematically illustrates a general, multistage reaction mechanism for aggregation that incorporates the putative steps inferred or deduced for a number of proteins (*21*−*24*, *29*, *32*−34). It is an adapted version of a more general scheme upon which the LENP mathematical model of non-native aggregation kinetics has been proposed and solved (*35*, *36*), including a number of simpler limiting cases (*33*, *37*−*41*). Scheme 1 shows a two-state folding pathway between native (*N*) and molten globule (*MG*) monomer states, with the aggregation-prone or reactive monomer species (*R*) assumed to be the molten globule. This is done for simplicity, and because it is relevant to a number of systems (*1*, *16*, *24*, *42*, *43*) and to the results presented in this article.

In Scheme 1, for an initially folded protein the first stage in the aggregation pathway is reversible unfolding to populate the reactive, non-native monomer state. The second stage is prenucleation, in which monomers (R) reversibly form oligomers (R_i) composed of i monomers ($i = 2, 3, ...$). The nucleation step (stage 3) involves an irreversible structural conversion or geometric rearrangement of an otherwise reversible oligomer composed of x monomers (R_x). This rearrangement step results in the smallest irreversible aggregate (A_x), and defines the nucleus size x as the number of monomers in R_x and A_x. If one assumes stage 3 to be rapid compared to the preceding step of $R + R_{x-1} \rightarrow R_x$, one instead obtains the simpler limiting case of association-limited nucleation (*37*, *38*, *44*, *45*). In that case, the nucleus size is effectively x-1. Stage 3 is explicitly included in Scheme 1 to capture situations in which the rate-limiting step for nucleation is an inter-protein rearrangement or alignment such as β-sheet formation.

To remain general and consistent with the physics of structure formation in the nucleation stage, aggregate growth via polymerization (stage 4 in Scheme 1) is treated as proceeding first by reversible association of δ unfolded monomers with an irreversible aggregate (A_j) composed of j monomers (typically $\delta = 1$ is assumed (*37*, *38*, *40*, *44*−*46*)). The reversible association step is followed by an irreversible structural transition or rearrangement of the R monomers that effectively commits them to the irreversible aggregate, now $A_{j+\delta}$. Aggregate polymerization can proceed for a given aggregate until its size reaches a threshold number of monomers, n^*. Once n^* is reached, the aggregates are able to appreciably participate in condensation steps (stage 5, Scheme 1) that result in precipitates or higher-order structures such as bundles, fibrils, gels, or amorphous precipitates.

In many cases, the kinetics of aggregation allow one to conclude that nucleation is thermodynamically unfavorable and that it therefore represents a rate-limiting step (*21*, *22*, *24*, *35*, *37*, *38*, *40*, *44*−*46*). In other cases a folding, unfolding, or association/dissociation step in stage 1 is rate-limiting (*33*, *34*, *47*−*50*), and therefore no information regarding pre-nucleation or growth can be inferred from experimental kinetics. Alternatively, if aggregates precipitate or condense at relatively low MW, information regarding nucleation but not growth can be inferred (*24*, *35*, *36*, *40*). In all cases, the location of the rate-limiting step(s) in the process and thus the key intermediates that govern the observed kinetics can depend on both the protein and the sample conditions of interest (*35*, *40*).

In Scheme 1, one can generally draw a distinction between aggregation-limited processes and (un)folding-limited ones. In the aggregation-limited case, assembly of non-native monomers is rate-limiting for monomer loss (i.e., stages 2−4, Scheme 1). Therefore, stage 1 can be treated as pre-equilibrated with respect to the later stages (*24*, *35*, *39*−*41*). In the (un)folding-limited case, aggregate assembly is rapid compared to folding or unfolding, and therefore the observed kinetics are either dominated by the dynamics of (un)folding (*33*, *34*, *48*) or are a convolution of assembly and (un)folding (*47*, *49*, *50*, *51*). Experimentally, the aggregation-limited and (un)folding-limited scenarios are most conclusively discerned by determining whether the observed aggregation time scale (e.g., the time to 50% loss of monomer, t_{50}) is significantly longer than that for folding−unfolding equilibration. In many cases, unfolding-limited kinetics also must be truly first order, with a rate coefficient that is independent of protein concentration (*24*, *34*, *35*).

For cases that are aggregation limited, key intermediates include R and the nucleus of x reactive monomers (R_x or A_x). In cases where x is two it is possible to conclude that the R monomer effectively is the (pre-)nucleus (*21*, *22*), or alternatively that aggregation is a downhill polymerization (*52*). Although the exact relationship between structure in the non-native state and its reactivity with respect to aggregation remains an outstanding challenge to address (*8*, *10*), for many proteins the reactive monomer conformational state is inferred from spectroscopy and/or mass spectrometry to be partially unfolded and possibly categorized as a molten globule (*1*, *8*, *10*, *16*, *24*, *42*, *43*, *53*, *54*).

Aggregate nuclei are even less well understood than monomer precursors, at least in part because nuclei and growing aggregates are often transient and relatively unstable. As a result, they are present at low levels compared to those

of monomers and downstream, larger aggregates. This makes them difficult to experimentally isolate and directly characterize. Indirect approaches, such as those based on interpretation of experimental aggregation kinetics (*21*, *22*, *24*, *32*, *35*−*37*, *40*, *52*), therefore provide a possible route to infer mechanistic details such as the number of monomers in the nucleus and the location of the rate-determining step(s).

To complete this section, we summarize key results from mathematical modeling of Scheme 1 that provide experimentally tractable expressions for the observed kinetics under aggregation-limited conditions. When aggregates remain soluble and grow via polymerization to significantly larger sizes than that of the nucleus, Scheme 1 leads to a seemingly simple rate equation for monomer loss when the reaction is monitored over approximately one or more half-lives (*35*, *36*, *40*).

$$\frac{dm}{dt} = -k_{obs} m^{\delta} \quad (1)$$

In eq 1, k_{obs} is the observed rate coefficient for a given temperature (T), pressure, solvent composition, and initial monomer concentration C_0. The fraction of monomer remaining is $m = [M]/C_0$, with $[M]$ denoting the monomer concentration at a given time t. The parameter δ was defined above as the number of monomers needed to propagate a growth step during polymerization. From eq 1, δ is also the apparent reaction order with respect to monomer concentration for the observed kinetics of monomer loss or aggregate conversion. As our results elsewhere (*35*, *36*) and analysis of simplified versions of Scheme 1 show (*23*, *37*, *38*, *40*), the value of k_{obs} from monomer loss or aggregate conversion kinetics over one or more half-lives is necessarily a convolution of stages 1−4. It can be written generally as (*35*, *36*)

$$k_{obs} = \left(\frac{C_0}{C_{ref}}\right)^{(x+d-1)/2} f_R^{(x+\delta)/2} \kappa \sqrt{\frac{1}{\tau_g^{(0)} \tau_n^{(0)}}} \quad (2)$$

In eq 2, κ is a constant close to one, and C_{ref} is an arbitrary reference or standard state protein concentration. Because stage 1 is rapid compared to later stages, the fraction of monomers in the reactive conformational state (f_R) is the same as its equilibrium value in the absence of aggregation. For a two-state protein in which U is equivalent to R, $f_R = f_U = K_{un}/(1 + K_{un})$ with K_{un} defined as the equilibrium constant for unfolding (cf., Scheme 1). Therefore, k_{obs} depends on the standard free energy of unfolding (ΔG^0_{un}) through f_R, with $K_{un} = \exp(-\Delta G^0_{un}/k_B T)$ and k_B denoting Boltzmann's constant.

The two remaining parameters in eq 2 are the intrinsic time scales for nucleation ($\tau_n^{(0)}$) and growth ($\tau_g^{(0)}$), both of which are functions of only temperature, pressure, and solvent composition. The intrinsic time scale for nucleation is equivalent to the inverse of the rate of nucleation when all monomers are present in the reactive conformation R, and the monomer concentration is fixed at a standard state or reference value (C_{ref}) (*36*). It is denoted as intrinsic because it is not a function of total protein concentration, folding−unfolding free energy or rate coefficients, or the fraction monomer remaining. The analogous quantity for growth is $\tau_g^{(0)}$ (*36*). $\tau_n^{(0)}$ and $\tau_g^{(0)}$ are each necessarily a product of two or more elementary rate coefficients or equilibrium constants that cannot easily be experimentally deconvoluted. Details of the derivation of eqs 1 and 2 as well as additional expressions of use in interpreting aggregation kinetics are provided in refs *35* and *36*.

The following points are notable from eq 2. First, if one works under native-favoring conditions the observed kinetics will necessarily have a significant and highly nonlinear contribution from ΔG^0_{un} because of the relationship between f_R and ΔG^0_{un}. Although it is possible to quantitatively factor out this contribution from experimental data (*24*), this can be difficult in many cases if aggregation at elevated temperatures complicates the use of thermal scanning techniques that are commonly used to determine ΔG^0_{un} for a given sample condition (*39*). With this consideration in mind, we selected solution conditions for aCgn aggregation such that aggregation kinetics could be practically measured at elevated temperatures in the absence of chemical denaturants. These conditions ensure that the fraction reactive or unfolded ($f_R = f_U$) is close to or essentially one and therefore permit us to focus on the contributions to aggregation from nucleation and growth over a range of temperatures.

Second, at fixed temperature, pressure, and solvent composition, all terms on the right-hand side of eq 2 except for $C_0^{(x+\delta-1)/2}$ are fixed. The value of δ is determined from the apparent reaction order with respect to monomer loss. A value for the nucleus size, x, can be determined by regressing experimental k_{obs} values against eq 2 over a range of initial monomer concentrations (C_0) at a given state point (*35*, *36*). A similar result for determining x from the C_0 dependence of aggregation kinetics can be obtained by a t^2 analysis of only the initial rates of monomer loss or aggregate conversion if one can obtain sufficiently high-resolution data over only the first 10 to 15% monomer loss (i.e., low extents of reaction) (*37*). When initial monomer loss is relatively rapid, it is often experimentally problematic or requires specialized experimental techniques (*55*, *56*) to obtain accurate and sufficient data over the early times of the reaction to reliably perform a t^2 analysis unless there is a pronounced accelerator character to the early-time kinetics (*22*, *55*, *56*).

Together, the preceding considerations motivate the approach adopted here of combining extensive quantitative data on folding−unfolding thermodynamics and dynamics, along with aggregation kinetics over multiple half-lives and a wide range of protein concentrations in order to infer details regarding the rate-limiting steps in aCgn aggregation. Spectroscopy and light scattering under selected conditions provide additional insight into questions of when structural conversion to β-sheet occurs within the kinetic aggregation scheme and whether it is required to maintain the integrity of the aggregates.

MATERIALS AND METHODS

Solution Preparation. 5× crystallized aCgn, 91 w/w % protein (manufacturer's analysis, lot number G8D212L) was purchased from Worthington Biochemical Corp. (Milford, MA) and used without further purification. Protein solutions were prepared gravimetrically at concentrations ranging from 0.05 to 4.0 mg/mL aCgn using 10 mM citrate buffer prepared from citric acid monohydrate (Fisher Scientific, Pittsburgh, PA, ACS grade) and water distilled in-house and deionized with a Millipore Corp. (Billerica, MA) Milli-Q filtration

system with a Quantum EX ultrapure organex cartridge. Total protein concentrations were consistent with analysis from direct UV absorbance at 280 nm. Buffer pH was adjusted to 3.5 with 1 M sodium hydroxide (Fisher Scientific, Pittsburgh, PA, molecular biology grade) prior to dissolving protein and rechecked after protein dissolution to ensure negligible changes. All protein samples had an initial concentration of nominal dimer or trimer of ca. 3% by area as determined from size-exclusion chromatography and the manufacturer's specification of 80 kDa upper MW cutoff for resolution on the column. Samples composed nominally of all aggregated protein were prepared by thermostatting initially monomeric protein solutions at 65 °C for a minimum of six times the half-life for monomer loss at the initial protein concentration of interest. Fully aggregated samples were quenched in an ice−water bath after preparation. Size-exclusion chromatography was used to verify that the monomer fraction remaining was less than 0.05 in all samples considered completely aggregated. All protein solutions (aggregated and unaggregated) were refrigerated (2−8 °C) and used within 1 week of preparation.

Preparation of Urea−Protein Solutions. Concentrated urea (8−10 M) stock solution in 10 mM sodium citrate buffer was prepared gravimetrically with urea (Fisher Scientific, Pittsburgh, PA, ACS grade), citric acid monohydrate (Fisher Scientific, Pittsburgh, PA, ACS grade), and deionized distilled water described above. Solution pH was adjusted to pH 3.5 with hydrochloric acid (Fisher Scientific, Pittsburgh, PA; certified ACS Plus grade). Urea stock solution was stored in a −20 °C freezer until used. Protein solutions at differing urea concentrations were prepared gravimetrically by dilution using the urea stock solution, protein stock solution at nominally 1.0 mg/mL, and pH 3.5 10 mM citrate buffer. Molarities were calculated using the polynomial expression for urea density as a function of molality and temperature (*57*). Protein solutions containing urea were stored at room temperature and used within 1 day of preparation.

Circular Dichroism (CD). Experiments were performed on a Jasco Inc. (Easton, MD) J-810 spectropolarimeter with a Jasco PTC-424S Peltier temperature controller. Spectra were obtained from 260 to 200 nm at a scanning rate of 50 nm/min in a 1 × 10 mm cuvette. Isothermal, equilibrium spectra were measured with 0.1 and 0.4 mg/mL aCgn samples from 20 to 80 °C in 5 °C increments. Samples were cooled after heating and the spectrum retaken to ensure reversibility. At each temperature, samples were allowed to equilibrate for 5 min prior to obtaining spectra, and a minimum of 3 spectra were taken and averaged. The corresponding buffer spectrum was subsequently subtracted. Mean residue ellipticity (MRE) in deg·cm^2/dmol was calculated from $\mathrm{MRE} = 0.1(\theta_\lambda)(\mathrm{MW})C_0^{-1}d^{-1}n_r^{-1}$ with θ_λ defined as the ellipticity in mdeg at wavelength λ, n_r denoting the number of amino acids per monomer, C_0 the solution concentration in mg/mL, d the cuvette path length in cm, and *MW* the monomer molecular weight in g/mol.

Differential Scanning Calorimetry (DSC). Experiments were performed with a VP-DSC (Microcal, Northampton, MA). A series of at least 5 buffer/buffer scans was used to establish instrument thermal history and to obtain the instrument baseline prior to each sample measurement. Samples of 0.2 mg/mL aCgn were heated from 20 to 90 °C at 60 °C/h. All samples were cooled and reheated to confirm reversibility. The corresponding buffer/buffer baseline was subtracted from each scan. The raw data were converted to absolute heat capacity using eq 3 (*58*)

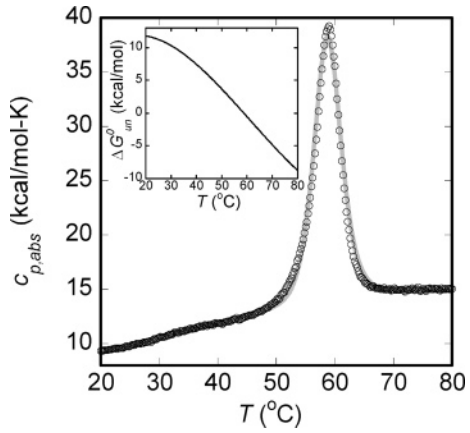

FIGURE 1: Absolute heat capacity of aCgn reversibly unfolded during thermal scanning in DSC at 60 °C/h (black circles) with two-state fit (gray line). The inset shows $\Delta G^0_{un}(T)$ calculated from the two-state fit of the DSC data.

$$\bar{c}_{\mathrm{p,abs}} = c_{\mathrm{p,w}}\frac{\bar{V}_{\mathrm{p}}}{\underline{V}_w} - \frac{\Delta c_{\mathrm{p,app}}}{m_{\mathrm{p}}} \tag{3}$$

where $\bar{c}_{p,abs}$ is the absolute, partial specific heat capacity of the protein, $c_{p,w}$ is the heat capacity of pure water, $\underline{V}_w$ *is* the specific volume of pure water, $\bar{V}_p$ *is* the partial specific volume of the protein, m_p is the mass of protein in the cell, and $\Delta c_{p,app}$ is the difference in DSC signal (scaled by scan rate) between the protein scan and the average buffer/buffer scan. Solvent properties were assumed to be essentially identical to those of pure water. $\bar{V}_p$ at 25 °C was 0.733 mL/g (*59*). The temperature dependence of $\bar{V}_p$ was calculated from Chalikian et al. (*31*) assuming negligible pH dependence between pH 2.0 and 3.5. Statistically indistinguishable values for the fitted parameters were obtained if this temperature dependence was neglected. Protein mass was calculated from $m_p = V_{cell}C_0$, where V_{cell} is the manufacturer's reported DSC cell volume. Data were converted to molar scales (monomer basis) for fitting and presentation.

The DSC data were regressed against a standard two-state model of folding/unfolding (*58*, *60*) assuming a linear temperature dependence of the partial molar heat capacity of native protein ($\bar{c}_{p,N}(T)$) and a temperature-independent partial molar heat capacity for the unfolded protein ($\bar{c}_{p,U}$). The regression provided fitted values and confidence intervals for the midpoint unfolding temperature (T_0), the enthalpy change (ΔH_0) of unfolding at T_0, $\bar{c}_{p,U}$, $\bar{c}_{p,N}$ ($T = 25$ °C), and the slope of $\bar{c}_{p,N}(T)$ with respect to temperature ($\mathrm{d}\bar{c}c_{p,N}/\mathrm{d}T$). The value of ΔG^0_{un} as a function of T was calculated from these parameters using standard thermodynamic analysis (*61*) while accounting explicitly for the T dependence of $\Delta c_{p,un}$ ($\equiv \bar{c}_{p,U} - \bar{c}_{p,N}(T)$) (*58*, *60*). Additional details are provided in the Appendix. The calorimetric enthalpy (ΔH_{cal}) was calculated by integrating the heat capacity data in Figure 1 with respect to temperature after subtracting the sigmoidal heat capacity baseline of the native to unfolded transition (*60*).

Size-Exclusion Chromatography (SEC). Monomer concentrations in solution were quantified using a Waters

Alliance 2695 separations module with a Waters 2996 photodiode array detector and Protein-Pak 7.8 × 300 mm size-exclusion column. Samples were maintained at 4 °C prior to injection, with the column held at room temperature, nominally 20−22 °C. The injection volume was either 100 μL or 50 μL; the smaller injection volume was used for samples with high protein concentration to avoid column overloading. The mobile phase (isocratic) was 0.5% (v/v) phosphoric acid (Fisher Scientific, Pittsburgh, PA, Certified ACS grade) in distilled deionized water adjusted to pH 2.5 with 5 M sodium hydroxide (*24*, *28*). The mobile phase flow rate was 1.0 mL/min. External calibration standards were made independently by mass, and run with each sample set. Monomer concentrations were calculated from peak area at 280 nm, integrated by the Empower software, and calibrated against the external standards over the linear range of detection for the standards.

Equilibrium Fluorescence. Measurements were performed with an ISS PC1 spectrofluorometer (ISS, Champaign, Illinois). Excitation and emission slit widths were 10 nm. Samples of 0.05 mg/mL aCgn were excited at 280 nm, with emission monitored from 300 to 450 nm in a 2 × 10 mm cuvette. The temperature of the sample unit was maintained at 26, 30, 34, or 38 °C (within 0.2 °C) with a circulating water bath. All samples were incubated directly in the bath prior to measurement to ensure equilibrium conditions. A minimum of 3 spectra were measured and averaged for each sample, with corresponding average buffer spectra subtracted after sample averaging. The spectral center of mass (COM) was calculated for each spectrum from eq 4 (*62*).

$$COM = \frac{\sum_{\lambda} (1/\lambda) I_{\lambda}}{\sum_{\lambda} I_{\lambda}} \tag{4}$$

where λ is the wavelength, and I_λ is the emission intensity at λ. The urea-unfolding COM data from each temperature were fit to a standard two-state model assuming linear pre- and post-transition baselines (*63*). The fit was performed globally using the nonlinear least-squares function *lsqcurvefit* in Matlab (The Mathworks, Natick, MA). The regressed parameters were the slopes and intercepts of the COM for each of the native and unfolded states, the m_{urea} value for urea dependence of ΔG^0_{un}, and the concentration (C_{mid}) of urea at which ΔG^0_{un} equals 0 for that temperature.

Stopped-Flow Fluorescence. Measurements were performed with an Applied Photophysics Spectrofluorimeter model SX.18MV-R (Applied Photophysics, Leatherhead, U.K.). Folding was induced by mixing equal volumes of protein in non-native-favoring urea concentrations with a solution of lower urea concentration to achieve a final, native-favoring urea concentration. The analogous but reverse procedure was used to induce unfolding. Folding/unfolding was monitored at 26, 30, 34, and 38 °C over a range of urea concentrations that bracketed the C_{mid} values determined independently from equilibrium fluorescence measurements. Fluorescence excitation was at 280 nm. The integrated emission signal was monitored over time with a 305 nm cutoff filter until either the signal reached a plateau or the maximum instrument monitoring time (1000 s) was reached. The temperature of the samples during the experiment was controlled to within 0.2 °C with an external circulating water bath. The data were regressed to a single exponential in Matlab to determine the apparent rate coefficient for equilibration of folding−unfolding (k_{u-f}) for each post-mixing urea concentration. Double-exponential fits were also considered but did not demonstrate an improvement over the single-exponential model under the conditions investigated here. The k_{u-f} values were used to construct Chevron plots at each temperature and were nonlinearly regressed against eqs 5−7 (*64*) using *lsqcurvefit* (Matlab). The regression provided values and confidence intervals at each temperature for the unfolding and folding rate coefficients at zero urea (k_u^0 and k_f^0, respectively) and for the corresponding m_{urea} values for the unfolding and folding branches of the profile (m_u and m_f, respectively).

$$\ln(k_u) = \ln(k_u^0) + m_u[\text{urea}] \tag{5}$$

$$\ln(k_f) = \ln(k_f^0) + m_f[\text{urea}] \tag{6}$$

$$\ln(k_{u-f}) = \ln(k_u + k_f) \tag{7}$$

Static Light Scattering (SLS). Samples with total protein concentration of 1.2 mg/mL were aggregated at 65 °C to greater than 95% aggregate and subsequently quenched in an ice−water bath or jumped to 80, 85, or 90 °C by manually transferring selected sample vials between water baths that were pre-equilibrated at the desired temperatures. Jumped samples were subsequently quenched on ice after hold times of 5, 10, or 30 min at the new temperature. Each sample was then diluted gravimetrically with buffer to concentrations of 0.05, 0.1, 0.2, 0.3, and 0.5 mg/mL. SLS measurements were made with a Brookhaven Instruments Corp. (Holtsville, NY) apparatus equipped with a Lexel model 95 Ar^- ion laser set at 488 nm, a BI9000AT correlator, and a BI200SM goniometer. All measurements were performed in a thermostatted cell at 20 °C. The weight average molecular weight ($\langle MW \rangle_w$) was determined from global regression of the scattered intensity against the Zimm equation (eq 8) (*65*) as a function of protein concentration (c, mass basis) and scattering angle (θ_{SLS}).

$$\frac{Kc}{R_{ex}} = \left(\frac{1}{\langle MW \rangle_w} + 2B_{22}c\right)\left(1 + \frac{q^2\langle R_g^2 \rangle_z}{3}\right) \tag{8}$$

where K is an optical constant defined as $K \equiv 4\pi^2 n^2 (dn/dc)^2 / N_A \lambda_0^4$, n is the refractive index, dn/dc is the refractive index increment of the protein solution (assumed to be 0.192 mL/g for aCgn), N_A is Avogadro's number, λ_0 is the laser wavelength *in vacuo*, R_{ex} is the excess Raleigh ratio defined as $R_{ex} \equiv (I - I_0/I_{ref})(n_0/n_{ref})^2 R_{ref}$, I is the scattered intensity, R_{ref} is the Raleigh ratio of toluene, B_{22} is the osmotic second virial coefficient, q is the magnitude of the scattering vector defined as $q \equiv 4\pi n \sin(\theta_{SLS}/2)/\lambda_0$, and $\langle R_g^2 \rangle_z$ is the z-average of the square of the radius of gyration. The subscripts *0* and *ref* on n and I denote quantities for buffer and toluene standard, respectively.

Monomer Loss Profiles. Monomer loss experiments were performed for samples with selected initial protein concentrations between 0.2 and 4.0 mg/mL at temperatures from

55 to 80 °C. Aliquots of 1.3 mL were pipetted into deactivated borosilicate glass HPLC vials (Waters, pn 186000272DV, total fill volume 1.5 mL), hermetically sealed with an unslit screw cap (Waters, pn 186000274) and incubated in a water bath at the desired temperature (within 0.2 °C). Each vial was removed after a selected incubation time and quenched by immediate manual immersion in an ice−water bath for a minimum of 5 min. Monomer concentration was determined from SEC as a function of incubation time for a given initial protein concentration and temperature. The data over ca. one or more half-lives were regressed against eq 1 for different integer values of δ (= 1, 2, 3,...) using a nonlinear least-squares algorithm (Matlab). Values and confidence intervals were obtained for each δ value for the two fitted parameters, k_{obs} and C_0. The latter parameter is implicit in the definition of m because data were collected as absolute monomer concentration [M]. The best fit was selected as that which minimized the relative 95% confidence intervals on k_{obs}, and maximized the randomness of the residuals. In practice, only $\delta = 1$ or 2 provided reasonable representations of monomer loss kinetics data at all conditions tested.

Temperature-Jump Depolymerization. Temperature-jump experiments were performed to quantify the depolymerization of aggregates at elevated temperatures. Samples with total protein concentrations of 1.2 mg/mL were incubated in a water bath at temperature T_1. The monomer loss profile at T_1 was generated as described in Monomer Loss Profiles. At a selected time, a set of vials were moved from the water bath at T_1 into a second water bath pre-equilibrated at a higher temperature T_2. Monomer recovery was monitored by removing samples at selected times from the water bath at T_2, quenching immediately in an ice−water bath, and quantifying monomer concentration with SEC.

RESULTS

Thermodynamics and Dynamics of Unfolding. The reversible unfolding transition of aCgn was evaluated with DSC, equilibrium fluorescence, stopped flow fluorescence, and CD. Figure 1 shows an equilibrium DSC scan using 0.2 mg/mL aCgn. The relatively low concentration was chosen to enable the unfolding transition to occur with less than 5% aggregation over the entire first scan, as determined by SEC and the lack of a significant scan-rate dependence in the DSC (not shown). The absolute heat capacity from eq 2 and the resulting two-state fit are shown. The unfolding transition is characterized by $\Delta G^0_{un}(T = 25\ °C) = 11.2 \pm 2.0$ kcal/mol, $\Delta H_0 = 144 \pm 1$ kcal/mol, $T_0 = 58.70 \pm 0.01$ °C, $\bar{c}_{p,N}(T = 25\ °C) = 9.8 \pm 0.1$ kcal/mol·K with a slope of 0.13 ± 0.01 kcal/mol·K^2, and $\bar{c}_{p,U} = 14.9 \pm 0.1$ kcal/mol·K.

Figure 2a shows a representative set of equilibrium fluorescence emission spectra at varying urea concentrations at 26 °C. Figure 2b shows equilibrium fluorescence COM as a function of [urea] at 26, 30, 34, and 38 °C. The curves are fits to the two-state model (see Materials and Methods) for each temperature. The regressed midpoint unfolding urea concentrations are C_{mid} = 4, 3.5, 3.2, and 2.6 M for 26, 30, 34, and 38 °C, respectively. The 95% confidence intervals of the fitted C_{mid} values in each case are no more than 5%. The m_{urea} value is essentially independent of temperature, with an average of 2.5 kcal/mol·M and a 95% confidence

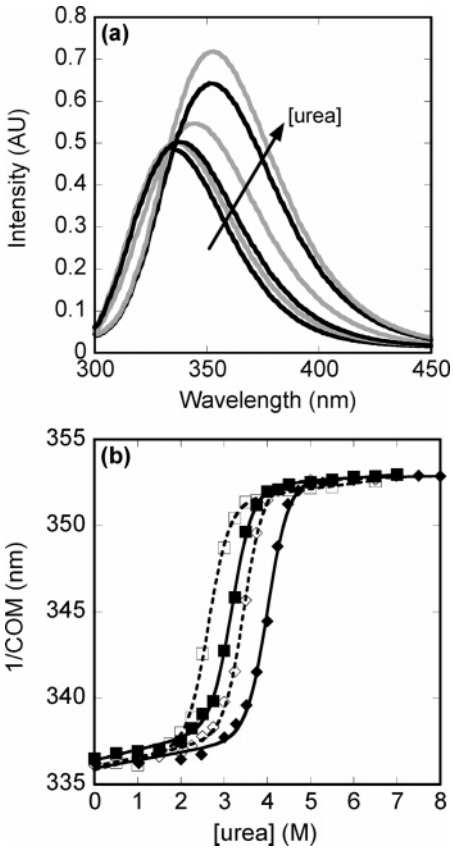

FIGURE 2: (a) aCgn fluorescence emission spectra at 26 °C for [urea] = 0, 3, 3.5, 4, 5, and 6 M. (b) Fluorescence center of mass as a function of urea concentration for monomer at 26 (♦), 30 (◇), 34 (■), and 38 °C (□). The lines are the corresponding fits to the two-state unfolding model.

Table 1: ΔG^0_{un} (kcal/mol) Values from Different Techniques[a]

T (°C)	DSC	equilibrium fluorescence	stopped-flow fluorescence
26	11.1 [9.3, 12.9]	9.9 [8.4, 11.4]	8.6 [6.9, 10.4]
30	10.3 [9.1, 11.5]	9.2 [8.1, 10.3]	7.3 [6.1, 8.4]
34	9.3 [8.6, 10.0]	8.1 [7.1, 9.1]	6.2 [4.5, 8.0]
38	8.1 [7.8, 8.4]	6.8 [5.4, 8.2]	6.3 [3.7, 8.9]

[a] The values in brackets indicate confidence intervals from global two-state model fits of the respective data sets. Both upper and lower bounds are shown because they are not necessarily symmetric about the mean due to the nonlinearity of the model equations. Entries are in the following format: value [upper bound, lower bound].

interval of 0.5 kcal/mol·M. The values of ΔG^0_{un} at zero [urea] along with the corresponding 95% confidence intervals are shown in Table 1.

Folding and unfolding rate coefficients were determined as a function of urea concentration by stopped-flow fluorescence at 26, 30, 34, and 38 °C. Representative time-course data along with the corresponding single-exponential fit are shown in Figure 3a. Figure 3b shows the resulting chevron curves for each temperature. The rate coefficient data in the chevron plots were fit as described in Materials and Methods to obtain values of the unfolding and refolding rate coefficients at 0 M urea. Using eq 9, ΔG^0_{un} values were determined from the stopped-flow data.

$$K_{un} = \exp\left(\frac{-\Delta G_{un}{}^0}{k_B T}\right) = \frac{k_u{}^0}{k_f{}^0} = \frac{\tau_f}{\tau_u} \qquad (9)$$

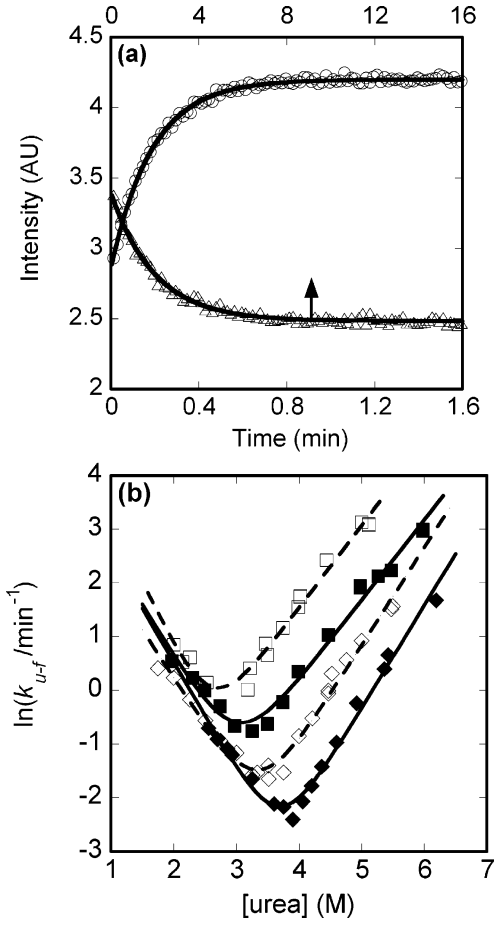

FIGURE 3: (a) Representative stopped-flow data for aCgn unfolding from 3 M urea to 6.1 M urea (○) and refolding from 5 M urea to 2.5 M urea (△) at 26 °C. (b) Chevron plot at 26 (♦), 30 (◊), 34 (■), and 38 °C (□). The error bars on all points are smaller than the symbols.

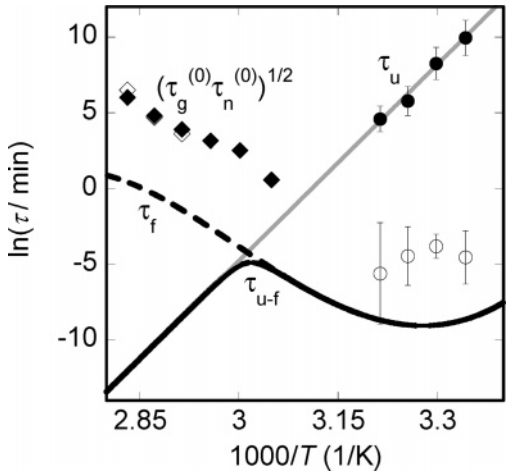

FIGURE 4: Folding−unfolding aggregation rate diagram. Experimental τ_u values (●), τ_f values (○), and $(\tau_g^{(0)}\tau_n^{(0)})^{1/2}$ values (♦, ◊) are overlaid with an Arrhenius fit of τ_u (gray line) and calculated curves for τ_{u-f} (black line) and τ_f (dashed line) as a function of inverse temperature based on eq 9.

These values are listed in Table 1 along with their 95% confidence intervals calculated from the confidence intervals on k_u^0 and k_f^0.

Figure 4 shows the characteristic time scales of unfolding and refolding as a function of inverse temperature, obtained from the corresponding rate coefficients at 0 M urea ($\tau_f = 1/k_f^0$, $\tau_u = 1/k_u^0$). The unfolding time scale or rate coefficient (τ_u in Figure 4) follows Arrhenius behavior. The refolding rate coefficient data do not exhibit a strong temperature dependence within statistical uncertainty. Therefore, the curve for refolding rate coefficients was calculated from eq 9 using the fitted values of k_u^0 from stopped-flow fluorescence, along with ΔG^0_{un} values as a function of temperature from the DSC data.

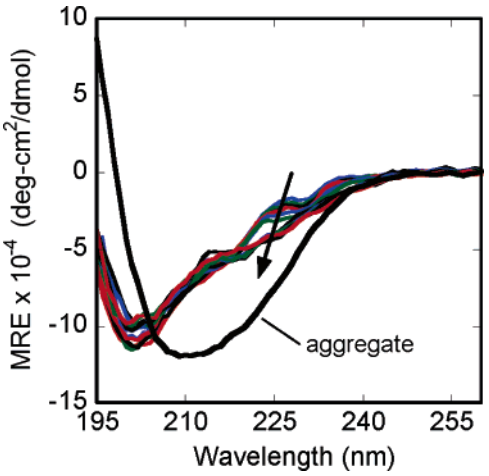

FIGURE 5: CD spectra of monomeric aCgn at temperatures from 20 to 80 °C in ca. 5 °C increments (colored lines), with the arrow indicating increasing temperature. The aggregate spectrum at 20 °C (black line) is shown for comparison.

Structural Changes upon Unfolding. Figure 2b shows the changes in fluorescence COM upon unfolding with urea at low temperatures ($T \ll T_0$), specifically a red shift with increasing [urea] that is indicative of increased solvent exposure of fluorescent side chains. The secondary structure changes accompanying the transitions from the native to unfolded state were monitored using far-UV CD. The spectra corresponding to the thermal unfolding of aCgn are shown in Figure 5. The wavelength corresponding to the maximum signal change is ca. 225 nm. Although not shown separately in Figure 5, $[\theta]_{225}$ as a function of temperature shows a distinct sigmoidal transition with a midpoint between 55 and 60 °C, in agreement with the calorimetric data. Compared to what is typically observed in far-UV CD when secondary structure is significantly disrupted upon unfolding (*66*, *67*), the changes in Figure 5 are relatively minor and quantitatively consistent with those reported previously for aCgn under similar conditions (*31*).

Structural Changes upon Aggregation. The spectrum of a fully aggregated sample is shown in Figure 5. Its signal is characteristic of β-sheet and is pronouncedly different from the native and unfolded spectra. The far-UV CD spectrum for the aggregate is essentially independent of temperature. Therefore, for clarity only the spectrum for 20 °C is shown in the Figure. Additional observations regarding the kinetics of β-sheet formation are included below (see Aggregate Dissociation).

Monomer Loss Kinetics. Monomer loss as a function of time was monitored with chromatography across a broad range of initial protein concentrations and temperatures. Illustrative chromatograms of selected time points are shown in Figure 6 from an isothermal incubation at 65 °C. All detectable aggregates that formed during incubation were found to coelute at ca. 6.5 mL, followed by the monomeric

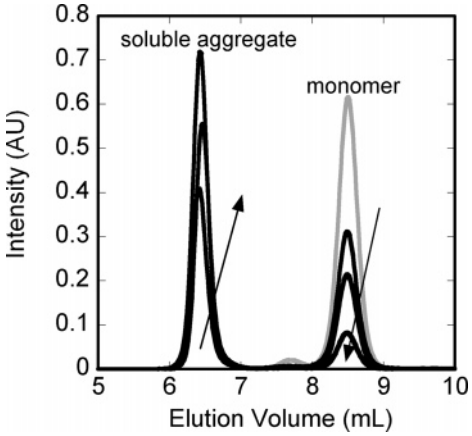

FIGURE 6: Illustrative HPLC chromatograms for samples quenched from incubation at elevated temperature. The arrows represent the direction of increasing incubation time.

protein at ca. 8.5 mL, and the buffer at ca. 11 mL. On the basis of previous data with the SEC method employed here (*24*, *28*), along with the manufacturer's specification of a 80 kDa MW cutoff, we estimate that all aggregates significantly larger than a trimer will co-elute. With the exception of the nominal dimer/trimer peak at a retention time of ca. 7.7 mL, we did not detect any species intermediate in size to the monomer and the lumped aggregate population in the peak at 6.5 mL. The peak at 7.7 mL is believed to be residual inactive species from purification during its commercial preparation, and it does not systematically correlate with monomer loss or growth of the 6.5 mL peak. Under all conditions used here, the 7.7 mL peak is essentially depleted before significant monomer loss occurs during incubation at elevated temperatures.

The inset in each panel of Figure 7 shows reduced monomer concentration ($m = [M]/C_0$) versus t/t_{50} for the temperature corresponding to its main panel, where t_{50} is the time for 50% loss of monomer ($m = 0.5$). Different symbols denote different concentrations for a single temperature. The data are plotted versus t/t_{50} to permit data on largely different time scales to be displayed simultaneously and to make qualitative similarities and differences in the time profiles more transparent. The value of t_{50} was determined via interpolation of the $m(t)$ data if the data extended past a half-life or from the fitted k_{obs} and C_0 values for conditions when aggregation proceeded too slowly to reach $m = 0.5$ before the experiment was halted. The solid lines in each plot are included as references to show the shape of perfect first-order or second-order kinetics when plotted as m versus t/t_{50}. The curves illustrate that typically the experimental data closely follow the first-order profile, except at elevated temperatures (75 and 80 °C) where the second-order profile is a better representation. Each monomer loss profile was regressed numerically against eq 1, as described in Materials and Methods, to determine which reaction order (δ) was statistically more appropriate as well as obtain the corresponding k_{obs} value and its statistical confidence interval.

Figure 8 shows k_{obs} as a function of temperature for each initial protein concentration. The aggregation rate coefficient is highly temperature dependent and has a maximum at or slightly below 65 °C at all protein concentrations studied. For comparison, the fraction of reactive or unfolded monomer

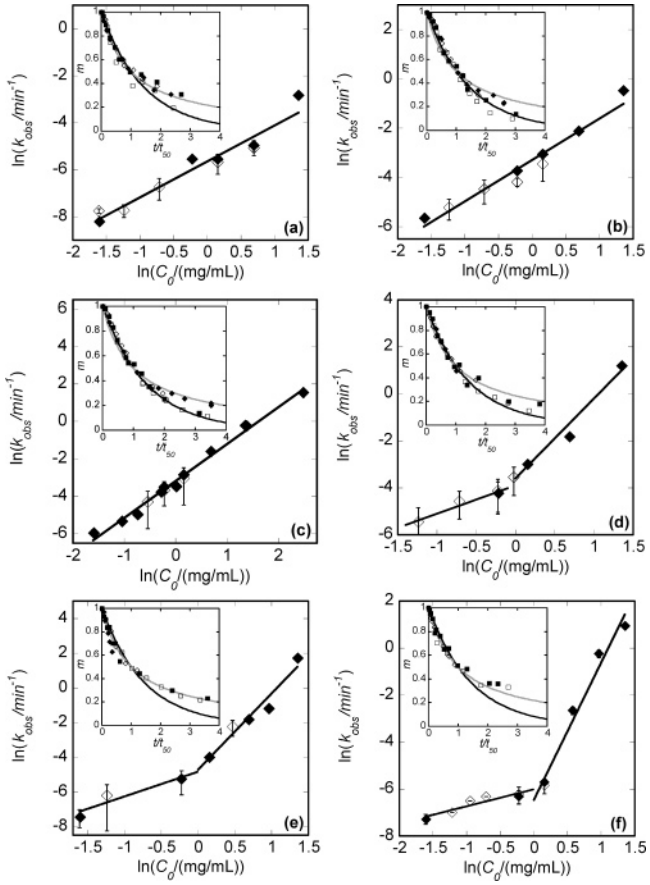

FIGURE 7: Monomer loss kinetics. Main panels: $\ln(k_{obs})$ vs $\ln(C_0)$ from full profiles (closed symbols) and initial rates (open symbols) at (a) 55 °C, (b) 60 °C, (c) 65 °C, (d) 70 °C, (e) 75 °C, and (f) 80 °C. Insets: monomer fraction vs t/t_{50} for 0.2 (♦), 0.8 (◇), 1.2 (■), and 2.0 mg/mL (□) for temperatures corresponding to the main panels. Only these four concentrations are shown for purposes of legibility. The lines in the insets represent purely first-order (black) and second-order (gray) kinetics.

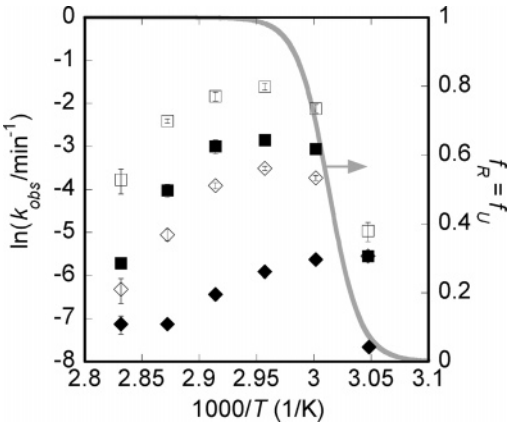

FIGURE 8: Comparison of k_{obs} and unfolded fraction of monomer vs inverse temperature for 0.2 (♦), 0.8 (◇), 1.2 (■), 2.0 mg/mL (□). The gray line shows $f_R = f_U$ calculated from DSC data.

($f_R = f_U = K_{un}/(1 + K_{un})$) is also shown in Figure 8. The f_U profile was calculated from the thermodynamic parameters of unfolding regressed from the DSC analysis described in Materials and Methods.

Concentration Dependence of k_{obs} and Determination of Nucleus Size (x). The dependence of k_{obs} on initial protein concentration (C_0) is shown in the main panels of Figure 7. Each panel corresponds to a different sample temperature.

Table 2: Nucleus Sizes (x) and the Number of Monomers in a Kinetic Event during Growth (δ) as a Function of Temperature[a]

T (°C)	δ	x
55	1	3 (1)
60	1	3 (1)
65	1	4 (1)
70	1	2 (1)
		7 (4)
75	2	2 (2)
		8 (3)
80	2	1 (1)
		11 (3)

[a] Symmetric confidence intervals for x from the linear regression of ln k_{obs} vs ln C_0 are given in parentheses. Entries with two x values list the value for the low-C_0 branch above that for the high-C_0 one.

A truly first order k_{obs} is independent of C_0 and would appear as a horizontal line in Figure 7.

In eq 2, the quantities f_R, $\tau_g^{(0)}$, and $\tau_n^{(0)}$ each are functions of only temperature, pressure, and solvent composition. Therefore, the slope of $\ln(k_{obs})$ versus $\ln(C_0)$ gives a value for $(x + \delta - 1)/2$ for each set of conditions in Figure 7. The value of δ is determined from the fit of the monomer loss profiles (see Monomer Loss Kinetics, Results section). The resulting x values can be calculated from the slopes in Figure 7 and are reported with their 95% confidence intervals in Table 2.

Aggregate Dissociation. Empirically, we observed that aCgn aggregates created during the monomer loss experiments described above dissociate if they are placed at elevated temperatures or intermediate concentrations of urea at ambient temperature, but do not dissociate upon cooling even when held for multi-week time scales. A detailed description of dissociation in urea is saved until a future report, but preliminary results show that sufficiently high concentrations of urea completely dissociate the aggregates to monomers that are able refold to the native structure, as detected by CD and fluorescence when subsequently dialyzed into native-favoring conditions.

The remainder of this section describes two temperature-jump experiments used to help assess whether β-sheet structure in the monomer is necessary to maintain an aggregated state and to characterize the relative enthalpies of the unfolded and aggregated states. Figure 9 shows the results for initially monomeric samples with $C_0 = 1.2$ mg/mL that were thermostatted at 75 °C, with selected samples jumped to 85 °C at 75 min before subsequent quenching. All samples were analyzed with SEC after quenching. The CD spectra of jumped and unjumped samples were also obtained at 20 °C after quenching and dilution to 0.4 mg/mL. The CD spectra were converted to apparent fraction of monomer remaining (m_{CD}) by regression against eq 10, which assumes that β-sheet formation requires a protein chain to be part of an aggregate (as detected by SEC).

$$\theta = m_{CD}\theta_m + (1 - m_{CD})\theta_A \qquad (10)$$

In eq 10, θ_m and θ_A are the reference spectra for monomer and aggregate, respectively, at 20 °C. In performing the regression, θ, θ_A, and θ_m are evaluated at all wavelengths between 260 and 205 nm, with a single value of m_{CD} as the fitting constant for a given sample. The resulting m_{CD} values are overlaid with the SEC values in Figure 9.

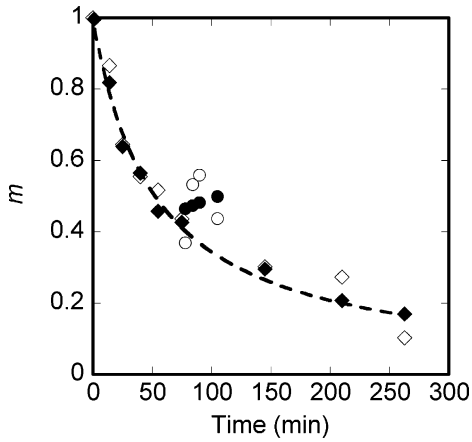

FIGURE 9: Monomer fraction vs time for $C_0 = 1.2$ mg/mL as measured by SEC (closed symbols) or by CD using eq 10 (open symbols). Samples were either held at 75 °C (♦, ◊) or held at 75 °C before being jumped to 85 °C (●, ○). The dashed line shows the fit of SEC data to eq 1 with $\delta = 2$.

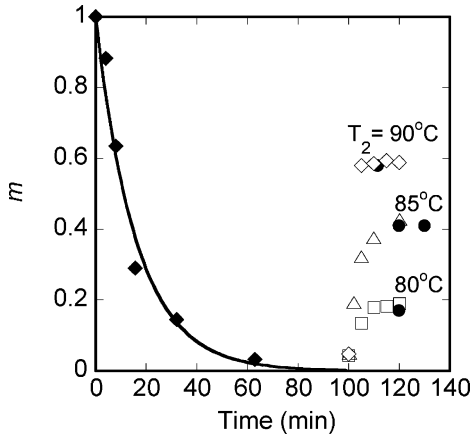

FIGURE 10: Monomer fraction (SEC) vs time for $C_0 = 1.2$ mg/mL held isothermally at 65 °C (♦) before jumping to 80 (□), 85 (△), and 90 °C (◊). The closed circles represent the calculated monomer fraction from SLS data (eq 11). The solid line is a fit of 65 °C data to eq 1 with $\delta = 1$.

Figure 10 shows a comparison of the results of a temperature-jump experiment monitored by chromatography and SLS. Samples were incubated at 65 °C for 100 min and then jumped to 80, 85, and 90 °C before subsequently quenching at later time points. The fraction of monomer remaining was quantified with chromatography for each sample. Selected samples at each temperature (indicated by ● in Figure 10) were additionally analyzed with SLS to determine the weight-averaged molecular weight. The pre-jump average aggregate size was 160 monomers; the post-jump average aggregate sizes were ca. 140, 100, and 70 monomers for jumps to 80, 85, and 90 °C, respectively. All reported aggregate sizes have 95% confidence intervals of no more than 10% of their reported values. A mass balance for monomer recovery based on the SLS measurements is given by eq 11.

$$m_{SLS} = m_1 + \frac{(\langle MW\rangle_{w,2} - \langle MW\rangle_{w,1})(1 - m_1)}{\langle MW\rangle_{w,1}} \qquad (11)$$

where the subscripts 1 and 2 denote temperature before and after the jump, respectively. This expression is valid only if the size distribution of aggregates has relatively low poly-

dispersity (weight avg./no. avg. ~1.5 or less), and the number concentration of aggregates is essentially unchanged by temperature jumping. The latter is equivalent to stipulating that no new aggregates are nucleated and that none of the previously formed aggregates are completely dissociated.

DISCUSSION

Folding-Unfolding Thermodynamics and Kinetics. The ΔG^0_{un} values from DSC are shown in the inset to Figure 1 over the temperature range in which experimental results are reported here. The values from DSC, equilibrium fluorescence, and stopped-flow measurements are provided for specific temperatures in Table 1. All values at a given temperature are the same within their respective 95% confidence intervals. In addition, the ratio of the calorimetric to van't Hoff enthalpy calculated from the fit of the DSC data shown in Figure 1 is 0.98 ± 0.01. These results, combined with the observation that both folding and unfolding show single-exponential kinetics in stopped-flow experiments across all temperatures and urea concentrations tested, indicate that a two-state model of unfolding is an accurate (macroscopic) representation (*68*, *69*) for aCgn at both high and low temperatures. The absolute heat capacity at 20 °C (9.3 ± 0.2 kcal·mol^{-1} K^{-1}) as well as the unfolding enthalpy and heat capacity change at T_0 are consistent with previous studies (*31*, *70*−*72*).

Based on the discussion regarding aggregation-limited versus unfolding-limited kinetics in the Introduction, we see from a comparison of the time scales in Figures 4 and 8 that aCgn aggregation is clearly aggregation-limited under all conditions here. The folding−unfolding time scale (Figure 4) is at least 2 orders of magnitude lower than that for even the fastest aggregation rates (k_{obs} maxima in Figure 8). It is notable that this observation is despite apparent first-order monomer loss kinetics over much of the temperature and C_0 conditions in Figure 7. In conjunction with the strong C_0 dependence of k_{obs}, these results provide a conclusive experimental illustration that (apparent) first-order aggregation kinetics on their own do not allow one to conclude that a monomolecular step such as unfolding is rate-limiting. The apparent first-order kinetics in the aggregation-limited case is instead an indication that aggregate growth occurs by monomer addition (*35*, *36*).

Conformational Changes upon Unfolding and Aggregation. The results in Figure 2 show that there is a significant fluorescence emission COM change accompanying unfolding, indicative of exposure of Trp and Tyr groups to the solvent, as expected when significant disruption of tertiary structure occurs (*66*, *67*). The spectra in Figure 2a show that fluorescence intensity generally increases upon unfolding in urea at low temperatures. This is in contrast to the expected decrease in intensity upon unfolding if the solvent acts to quench fluorescence relative to the apolar protein interior (*66*, *67*) but has been observed in other systems (*73*). This behavior for aCgn has been previously observed by Poklar et al. (*74*), although its precise structural basis does not appear to be conclusively known. Overall, our data and those of others for thermal unfolding under similar conditions (*31*) indicate a significant and cooperative loss of tertiary structure for aCgn upon unfolding.

Figure 5 indicates that only subtle changes in secondary structure occur between the native and unfolded states, as detected by far-UV CD. These changes occur cooperatively over a narrow temperature range that corresponds to the unfolding endotherm measured in DSC. These observations indicate the unfolded state of aCgn retains much of the native secondary structure. Taken together with the observation that a significant and cooperative loss of tertiary structure occurs upon unfolding, our data indicate the unfolded state of aCgn is essentially that of a molten globule at the acidic pH conditions employed here. These observations are also consistent with previous thermal unfolding studies of aCgn at acidic pH (*30*, *31*), and the native crystal structure of aCgn in which a large fraction of amino acids are not clearly classified as helix or sheet (*75*).

In contrast to the structural changes upon unfolding, the aggregate spectrum has a characteristic β-sheet profile typical of non-native aggregates. Furthermore, the evolution of the CD-detected monomer levels (Figure 9) quantitatively aligns with SEC-detected monomer loss and recovery before and after a temperature jump, respectively. Together with the small changes in CD-detected secondary structure for monomer unfolding, these observations suggest that β-sheet conversion predominantly occurs upon aggregation, rather than occurring as a stable structure in the monomer precursor to aggregation. Without being able to isolate reversible aggregates (i.e., R_i, $i = 2, ..., x$ in Scheme 1), it is not possible to conclusively determine if β-sheet is present in only the irreversible aggregates (A_j in Scheme 1) or also in the reversible species. The quantitative and semi-quantitative agreement between CD- and SEC-monitored monomer loss and recovery further confirms the observation from SEC that no prenuclei or reversible non-native oligomers are sufficiently populated to be detectable with bulk assays. Finally, as discussed below, the majority of monomer consumption or recovery, respectively, is due to growth or depolymerization of existing aggregates under the conditions in Figures 9 and 10. Thus, it is reasonable to conclude that β-sheet conversion occurs as part of the rate-determining step in growth or that it occurs very soon after that step.

Negative Activation Energies and Intrinsic Timescales of Nucleation and Growth. Equation 2 shows that the observed rate coefficient for aggregation under aggregation-limited conditions depends on essentially three contributions: the equilibrium fraction unfolded or reactive fraction of monomers ($f_U = f_R$) raised to the power $(x + \delta)/2$; the ratio C_0/C_{ref} raised to the power $(x + \delta - 1)/2$; and an intrinsic time scale of aggregation defined as the geometric mean of the intrinsic time scales for nucleation and growth, $(\tau_g^{(0)}\tau_n^{(0)})^{1/2}$. The value of f_U was calculated as a function of temperature from the thermodynamic parameters regressed from DSC, as described in the Results section regarding Figure 8. The values of x and δ for each temperature and C_0 were determined as described in the Results section using the data in Figure 7. We selected a reference concentration $C_{ref} = 1$ mg/mL (= 38.9 μM, monomer basis) to determine the C_0/C_{ref} contributions for each condition. The f_U and C_0 contributions were then factored out from each k_{obs} value to provide values of $(\tau_n^{(0)}\tau_g^{(0)})^{1/2}$. The inverse of this quantity is essentially the intrinsic rate coefficient for aggregation. Recall that the intrinsic values are those under reference conditions where all monomers are in the unfolded or reactive conformational state and the monomer concentration is set

at C_{ref}. The values obtained by this procedure are shown as diamonds in Figure 4.

From Figure 4, we see that the intrinsic aggregation rate coefficient decreases with increasing temperature (i.e., $(\tau_n^{(0)}\tau_g^{(0)})^{1/2}$ increases as $1/T$ decreases) and this therefore indicates a negative net activation energy. At fixed C_0, there are only two temperature-dependent terms in k_{obs}: $(\tau_n^{(0)}\tau_g^{(0)})^{1/2}$ and f_R ($= f_U$). The derivative of ln f_U with respect to T is necessarily positive and approaches zero when T is significantly higher than T_0 (*60*). This is also evident from the f_U curve in Figure 8. At T more than a few degrees above T_0, f_U is essentially one, but below this it is a strongly increasing function of temperature. Thus, the maximum in k_{obs} with temperature is due to a competition between the temperature dependence of the folding−unfolding equilibrium and that of the intrinsic rate coefficient for aggregation. The former contribution dominates at lower T and causes k_{obs} to strongly increase with T below approximately T_0. The latter dominates at higher T and results in the net negative activation energy significantly above T_0.

The physical reason for the increase in $(\tau_n^{(0)}\tau_g^{(0)})^{1/2}$ with increasing temperature cannot be unambiguously deduced from the available data. This is at least in part because $(\tau_n^{(0)}\tau_g^{(0)})^{1/2}$, or equivalently k_{obs}, contains information about both nucleation and growth. This is a problem common to all kinetic rate coefficients that are extracted from data such as monomer loss, aggregate mass conversion, overall dye binding to aggregate, and turbidity. This convolution is also independent of whether one uses initial-rates or t^2 analysis (*21*, *22*, *37*), or bases the analysis on kinetics measured over one or more half-lives (*35*, *36*, *38*). We instead simply note that our data in Figures 9 and 10 suggest β-sheet conversion is part of the rate-limiting step for growth and that the characteristic folding time (τ_f) for aCgn also displays a negative activation energy of similar magnitude over the same range of temperature in Figure 4. The data are therefore suggestive but not conclusive that the processes of folding and structural conversion as part of nucleation and growth have some common kinetic features. If this similarity has a mechanistic basis, then by analogy to folding it suggests the structural conversion to β-sheet during aggregation (after monomer unfolding) has a significant entropic barrier at high temperatures but may be dominated by an enthalpic barrier at lower temperatures (*76*, *77*).

In an effort to help elucidate the effects of temperature on aggregate stability and aggregation kinetics, a series of temperature-jump experiments from T_1 (starting temperature) to T_2 (ending temperature before quenching on ice) were performed as described in Materials and Methods. The quantitative agreement between monomer loss/recovery by SEC and CD are consistent with a viewpoint in which β-sheet structures are a key stabilizing factor in maintaining the aggregated state. Furthermore, the quantitative agreement in Figure 10 between the amount of monomer recovered, as determined chromatographically, versus that inferred by measuring changes in the aggregate $\langle MW\rangle_w$ before and after temperature jumping can hold only if the number concentration of aggregates is essentially unchanged by the depolymerization process. Thus, we conclude that aggregate dissociation occurs primarily via incomplete depolymerization of the existing aggregates and that few or no aggregates are fully depolymerized.

This last result is important in that it indicates the temperature-jump data inform on the relative energetics of the growth phase (stage 4 in Scheme 1), without being convoluted by reversal of the nucleation stage. Bearing this in mind, from LeChatelier's principle the dissociation of aggregates upon temperature jumping indicates the enthalpy of aggregates (after nucleation) is significantly lower than the enthalpy of the unfolded monomer. Based on only the present results, it is not possible to quantitatively determine this enthalpy difference or compare it to the difference between folded and unfolded monomer determined from DSC. However, our preliminary data indicate it is sufficiently large to be detected during DSC experiments at higher protein concentrations than those used to generate Figure 1 (Andrews, J., and Roberts, C., unpublished work). A more detailed investigation of this behavior is currently being completed and will be provided in a future report.

Nucleation Occurs through More than One Nucleus Size. Table 2 shows the x values obtained for each temperature from the regression of data in Figure 7 (main panels) against eq 2, with δ set by the apparent reaction order for monomer loss versus t/t_{50} (insets in Figure 7). The most striking observations in Figure 7 and Table 2 are: (1) at sufficiently high temperatures (70 °C and above), there are two statistically different x values corresponding to distinct branches in the ln k_{obs} versus ln C_0 profiles; (2) the dominant nucleus size for the high-C_0 branch (high T only) increases with increasing temperature and is always greater than that for the low-C_0 branch; and (3) within statistical uncertainty, the dominant nucleus size for the low-C_0 branch is between two and four for all temperatures. These results are noteworthy, considering that it is common practice to assume a simpler scenario in which only one x value need be considered for a given protein or solution condition.

Preliminary calculations with a version of our LENP model in which two nucleus sizes (x and x', $x < x'$) compete with each other show behavior equivalent to that shown in Figure 7d−f. Specifically, the model predicts two distinct linear regimes for ln k_{obs} versus ln C_0, provided x and x' differ by a value of 3 or more. Therefore, although our data at lower temperatures do not show two distinct branches within statistical uncertainty, we do not anticipate the resolution of our k_{obs} values versus C_0 is sufficient to discern a difference in x and x' smaller than those found here for 70 °C and above. Thus, it is possible that two competing nucleus sizes exist below 70 °C, but the size of the larger one approaches that of the smaller one as temperature is reduced.

The physical reason for two competing nucleus sizes is not known at this point. We speculate that in principle any non-native oligomer size could be the nucleus but that certain stoichiometries or cluster numbers have more favorable monomer−monomer contacts or permit larger, cooperative structural fluctuations to occur, and these characteristics make the structural conversion to β-sheet or the formation of cooperative, strong inter-protein contacts more facile. It is also conceivable that different nucleus sizes will give rise to different aggregate morphologies. It is notable that the larger nuclei are suppressed by lowering the temperature. This might be because they are higher in enthalpy than the smaller nuclei and therefore are preferentially stabilized by increasing temperature. However, it might also be simply because the concentration of nuclei are proportional to

reactive monomer concentration to the power x or x'. If the reactive monomer conformational state is not N, then as one lowers the temperature the reactive monomer will be rapidly depopulated, and larger nuclei will be destabilized to a greater degree than smaller nuclei.

Finally, it is also notable that having two distinct competing nucleus sizes rather than a continuous shift in effective nucleus with increasing concentration is a result that cannot be obtained if one simply treats the rate-limiting step for nucleation as a size-independent association step for $R + R_{x-1} \rightarrow R_x$. This can be seen by contrasting our results with those of previous experimental (*55*, *56*) and theoretical (*45*) work. If the rate-limiting step for nucleation is simply the addition of another monomer to a prenucleus, then increasing C_0 can produce a continuous change in nucleus size as concentration increases. That is, the slope of ln k_{obs} versus ln C_0 changes smoothly (*45*, *55*, *56*) rather than making a discrete jump from one value to another. To the best of our knowledge, the findings here regarding two distinct competing nucleus sizes that involve conformational rearrangement to nucleate have not been previously reported by other workers.

SUMMARY AND CONCLUSIONS

Key intermediates in the non-native aggregation pathway of aCgn under acidic, accelerated conditions (pH 3.5 and elevated temperatures) were determined from a combination of experiment and model analysis, including: monomer loss kinetics; temperature jumps to induce aggregate dissociation; thermodynamics, kinetics, and structural changes upon (un)-folding; and scaling of aggregation rate coefficients with protein concentration. The reactive or aggregation-prone conformational state for aCgn monomers under these conditions is found to be a molten globule, similar to what has been inferred or shown for other systems. The rate-limiting steps for aggregation are nucleation and growth, and growth occurs primarily by addition of one or two monomers per kinetic event. The nucleus size ranges from 2 to over 10, depending on initial protein concentration and temperature. Unlike in previous studies where multiple nucleus sizes have been inferred, our data are consistent with there being predominantly two competing nucleus sizes and nucleation involving a cooperative conformational transition within the nucleus rather than simply the addition of a free monomer to a smaller prenucleus. These results, combined with quantitative comparison of the kinetics of monomer loss and β-sheet conversion, suggest the rate-limiting steps in nucleation and/or growth involve β-sheet conversion after monomers have reversibly associated with each other (prenucleation) or with previously formed irreversible aggregates.

The observed or overall rate coefficient for aggregation has a maximum a few degrees above the midpoint unfolding temperature, due to competition between the temperature shift in folding−unfolding equilibrium and the decrease in intrinsic aggregation rates with increasing temperature. The intrinsic aggregation rate coefficient has a negative activation energy, similar to that for folding, suggesting some level of analogy between the entropic and enthalpic bottlenecks for folding and the conformational changes to non-native, β-sheet structure in the aggregates. Finally, the aggregates formed by incubation of molten globule aCgn can be depolymerized on the time scale of minutes at elevated temperatures, consistent with protein chains in the aggregates being significantly lower in enthalpy than molten globule monomers under the same conditions.

ACKNOWLEDGMENT

We thank Dr. A. S. Robinson for use of the ISS fluorimeter and W. F. Weiss IV for the Matlab code used to fit the equilibrium fluorescence data and the SLS data, as well as for aid with the SLS measurements. We also thank Dr. E. W. Kaler for use of the light scattering equipment.

APPENDIX: UNFOLDING THERMODYNAMICS FROM DSC

The native and unfolded partial molar heat capacities are given by eqs A1 and A2, in which a, $\bar{c}_{p,N,0}$, and $\bar{c}_{p,U,0}$ are temperature-independent.

$$\bar{c}_{p,N} = aT + \bar{c}_{p,N,0} \quad \text{(A1)}$$

$$\bar{c}_{p,U} = \bar{c}_{p,U,0} \quad \text{(A2)}$$

The heat capacity difference upon unfolding at any given T is defined as $\Delta c_p(T) = \bar{c}_{p,U} - \bar{c}_{p,N}$, and the subscript *0* in eqs A1 and A2 denotes that the value is independent of temperature. For the native heat capacity, 25 °C was taken as the reference temperature. The differences between unfolded and native state enthalpy and entropy follow, respectively, from eqs A3 and A4.

$$\Delta H_{un}(T) \equiv \bar{H}_U(T) - \bar{H}_N(T) = \Delta H_0 + \int_{T_0}^{T} \Delta c_p(T) dT \quad \text{(A3)}$$

$$\Delta S_{un}(T) \equiv \bar{S}_U(T) - \bar{S}_N(T) = \Delta S_0 + \int_{T_0}^{T} \frac{\Delta c_p}{T} dT = \frac{\Delta H_0}{T_0} + \int_{T_0}^{T} \frac{\Delta c_p}{T} dT \quad \text{(A4)}$$

The value of T_0 is taken here as that at which $\Delta G^0_{un} = 0$. The right most expression in eq A4 includes the substitution $\Delta S_0 = \Delta H_0/T_0$ from this definition of T_0. The protein heat capacity as a function of temperature is then

$$\bar{c}_{p,abs}(T) = \bar{c}_{p,N}(T) + f_U \Delta c_p(T) + \Delta H_{un}(T) \frac{df_U}{dT}\Big|_T \quad \text{(A5)}$$

with f_U given by eq A6, df_U/dT given by eq A7, and the subscript T in eq A7 denoting that the derivative is evaluated locally at T.

$$f_U = \frac{\exp(-\Delta G_{un}{}^0/k_B T)}{1 + \exp(-\Delta G_{un}{}^0/k_B T)} \quad \text{(A6)}$$

The derivative of f_U with respect to temperature is

$$\frac{df_U}{dT}\Big|_T = \frac{f_U(1 - f_U)\Delta H_{un}}{RT^2} \quad \text{(A7)}$$

Equations A1−A7 were used to globally fit the DSC data with model parameters ΔH_0, T_0, $a = (d\bar{c}_{p,N}/dT)$, $\bar{c}_{p,N,0}$, and $\bar{c}_{p,U,0}$.

REFERENCES

1. Fink, A. L. (1998) Protein aggregation: folding aggregates, inclusion bodies and amyloid, *Folding Des. 3*, R9−R23.

2. Eisenberg, D., Nelson, R., Sawaya, M. R., Balbirnie, M., Sambashivan, S., Ivanova, M. I., Madsen, A. O., and Riekel, C. (2006) The structural biology of protein aggregation diseases: fundamental questions and some answers, *Acc. Chem. Res. 39*, 568−575.
3. Booth, D., Sunde, M., Bellotti, V., Robinson, C., Hutchinson, W., Fraser, P., Hawkins, P., Dobson, C., Radford, S., Blake, C., and Pepys, M. (1997) Instability, unfolding and aggregation of human lysozyme variants underlying amyloid fibrillogenesis, *Nature 385*, 787−793.
4. Ronga, L., Tizzano, B., Palladino, P., Ragone, R., Urso, E., Maffia, M., Ruvo, M., Benedetti, E., and Rossi, F. (2006) The prion protein: structural features and related toxic peptides, *Chem. Biol. Drug Des. 68*, 139−147.
5. Rousseau, F., Schymkowitz, J., and Serrano, L. (2006) Protein aggregation and amyloidosis: confusion of the kinds? *Curr. Opin. Struct. Biol. 16*, 118−126.
6. McAllister, C., Karymov, M. A., Kawano, Y., Lushnikov, A. Y., Mikheikin, A., Uversky, V. N., and Lyubchenko, Y. L. (2005) Protein interactions and misfolding analyzed by AFM force spectroscopy, *J. Mol. Biol. 354*, 1028−1042.
7. Sunde, M., Serpell, L., Bartlam, M., Fraser, P., Pepys, M., and Blake, C. (1997) Common core structure of amyloid fibrils by synchrotron X-ray diffraction, *J. Mol. Biol. 273*, 729−739.
8. Dobson, C. M. (2004) Principles of protein folding, misfolding and aggregation, *Semin. Cell Dev. Biol. 15*, 3−16.
9. Pochan, D. J., Schneider, J. P., Kretsinger, J., Ozbas, B., Rajagopal, K., and Haines, L. (2003) Thermally reversible hydrogels via intramolecular folding and consequent self-assembly of a de novo designed peptide, *J. Am. Chem. Soc. 125*, 11802−11803.
10. Uversky, V. N., and Fink, A. L. (2004) Conformational constraints for amyloid fibrillation: the importance of being unfolded, *Biochim. Biophys. Acta 1698*, 131−153.
11. Cleland, J., Powell, M., and Shire, S. (1993) The development of stable protein formulations- a close look at protein aggregation, deamidation, and oxidation, *Crit. Rev. Ther. Drug Carrier Syst. 10*, 307−377.
12. Remmele, R., Bhat, S., Phan, D., and Gombotz, W. (1999) Minimization of recombinant human Flt3 ligand aggregation at the T-m Plateau: a matter of thermal reversibility, *Biochemistry 38*, 5241−5247.
13. Purohit, V. S., Middaugh, C. R., and Balasubramanian, S. V. (2006) Influence of aggregation on immunogenicity of recombinant human Factor VIII in hemophilia A mice, *J. Pharm. Sci. 95*, 358−371.
14. Rosenberg, A. S. (2006) Effects of protein aggregates: an immunologic perspective, *AAPS J. 8*, E501−E507.
15. Cromwell, M. E. M., Hilario, E., and Jacobson, F. (2006) Protein aggregation and bioprocessing, *AAPS J. 8*, E572−E579.
16. Middaugh, C. R., and Edwards, K. L. (1998) Recent advances in our understanding of protein conformational stability from a pharmaceutical perspective, *Expert Opin. Invest. Drugs 7*, 1493−5000.
17. Ross, C., and Poirier, M. (2004) Protein aggregation and neurodegenerative disease, *Nat. Med.* S10−S17.
18. Murphy, R. M., and Tsai, A. M. (2006) Protein Folding, Misfolding, Stability, and Aggregation: An Overview, in *Misbehaving Proteins: Protein Misfolding, Aggregation, and Stability* (Murphy, R. M., and Tsai, A. M., Eds.), Springer, New York.
19. Gibson, T. J., and Murphy, R. M. (2006) Inhibition of insulin fibrillogenesis with targeted peptides, *Protein Sci. 15*, 1133−1141.
20. Kirkitadze, M., Condron, M., and Teplow, D. (2001) Identification and characterization of key kinetic intermediates in amyloid beta-protein fibrillogenesis, *J. Mol. Biol. 312*, 1103−1119.
21. Chen, S., Ferrone, F. A., and Wetzel, R. (2002) Huntington's disease age-of-onset linked to polyglutamine aggregation nucleation, *Proc. Natl. Acad. Sci. U.S.A. 99*, 11884−11889.
22. Ignatova, Z., and Gierasch, L. M. (2005) Aggregation of a slow-folding mutant of a beta-clam protein proceeds through a monomeric nucleus, *Biochemistry 44*, 7266−7274.
23. Lomakin, A., Chung, D., Benedek, G., Kirschner, D., and Teplow, D. (1996) On the nucleation and growth of amyloid beta-protein fibrils: detection of nuclei and quantitation of rate constants, *Proc. Natl. Acad. Sci. U.S.A. 93*, 1125−1129.
24. Roberts, C. J., Darrington, R. T., and Whitley, M. B. (2003) Irreversible aggregation of recombinant bovine granulocyte-colony stimulating factor (bG-CSF) and implications for predicting protein shelf life, *J. Pharm. Sci. 92*, 1095−1111.
25. Tartaglia, G., Cavalli, A., Pellarin, R., and Caflisch, A. (2005) Prediction of aggregation rate and aggregation-prone segments in polypeptide sequences, *Protein Sci. 14*, 2723−2734.
26. Fernandez-Escamilla, A. M., Rousseau, F., Schymkowitz, J., and Serrano, L. (2004) Prediction of sequence-dependent and mutational effects on the aggregation of peptides and proteins, *Nat. Biotechnol. 22*, 1302−6.
27. DuBay, K. F., Pawar, A. P., Chiti, F., Zurdo, J., Dobson, C. M., and Vendruscolo, M. (2004) Prediction of the absolute aggregation rates of amyloidogenic polypeptide chains, *J. Mol. Biol. 341*, 1317−26.
28. Bartkowski, R. E., Kitchel, R., Peckham, N. R., and Margulis, L. (2002) Aggregation of recombinant bovine granulocyte colony stimulating factor in solution, *J. Protein Chem. 21*, 137−143.
29. Remmele, R. L., Jr., Zhang-van Enk, J., Dharmavaram, V., Balaban, D., Durst, M., Shoshitaishvili, A., and Rand, H. (2005) Scan-rate-dependent melting transitions of interleukin-1 receptor (type II): elucidation of meaningful thermodynamic and kinetic parameters of aggregation acquired from DSC simulations, *J. Am. Chem. Soc. 127*, 8328−8339.
30. Brandts, J., and Lumry, R. (1963) Reversible thermal denaturation of chymotrypsinogen. 1. Experimental characterization, *J. Phys. Chem. 67*, 1484−1494.
31. Chalikian, T. V., Volker, J., Anafi, D., and Breslauer, K. J. (1997) The native and the heat-induced denatured states of alpha-chymotrypsinogen A: thermodynamic and spectroscopic studies, *J. Mol. Biol. 274*, 237−252.
32. Pallitto, M. M., and Murphy, R. M. (2001) A mathematical model of the kinetics of beta-amyloid fibril growth from the denatured state, *Biophys. J. 81*, 1805−1822.
33. Kendrick, B. S., Cleland, J. L., Lam, X., Nguyen, T., Randolph, T. W., Manning, M. C., and Carpenter, J. F. (1998) Aggregation of recombinant human interferon gamma: kinetics and structural transitions, *J. Pharm. Sci. 87*, 1069−1076.
34. Sanchez-Ruiz, J. M., Lopez-Lacomba, J. L., Cortijo, M., and Mateo, P. L. (1988) Differential scanning calorimetry of the irreversible thermal denaturation of thermolysin, *Biochemistry 27*, 1648−1652.
35. Roberts, C. J. (2006) Non-Native Protein Aggregation: Pathways, Kinetics, and Stability Prediction, in *Misbehaving Proteins: Protein Misfolding, Aggregation, and Stability* (Murphy, R. M., and Tsai, A. M., Eds.), Springer, New York.
36. Andrews, J. M., and Roberts, C. J. (2007) A Lumry-Eyring nucleated-polymerization (LENP) model of protein aggregation kinetics I. Aggregation with pre-equilibrated unfolding, *J. Phys. Chem. B*, in press.
37. Ferrone, F. (1999) Analysis of Protein Aggregation Kinetics, in *Amyloid, Prions, and Other Protein Aggregates* (Wetzel, R., Ed.) pp 256−274, Academic Press, San Diego, CA.
38. Oosawa, F., and Asakura, S. (1975) *Thermodynamics of the Polymerization of Proteins*, Academic Press, London.
39. Sanchez-Ruiz, J. M. (1992) Theoretical analysis of Lumry-Eyring models in differential scanning calorimetry, *Biophys. J. 61*, 921−935.
40. Roberts, C. J. (2003) Kinetics of irreversible protein aggregation: Analysis of extended Lumry-Eyring models and implications for predicting protein shelf life, *J. Phys. Chem. B 107*, 1194−1207.
41. Zale, S. E., and Klibanov, A. M. (1983) On the role of reversible denaturation (unfolding) in the irreversible thermal inactivation of enzymes, *Biotechnol. Bioeng. 25*, 2221−2230.
42. Grillo, A., Edwards, K., Kashi, R., Shipley, K., Hu, L., Besman, M., and Middaugh, C. (2001) Conformational origin of the aggregation of recombinant human factor VIII, *Biochemistry 40*, 586−595.
43. Hammarstrom, P., Persson, M., Freskgard, P. O., Martensson, L. G., Andersson, D., Jonsson, B. H., and Carlsson, U. (1999) Structural mapping of an aggregation nucleation site in a molten globule intermediate, *J. Biol. Chem. 274*, 32897−32903.
44. Goldstein, R. F., and Stryer, L. (1986) Cooperative polymerization reactions. Analytical approximations, numerical examples, and experimental strategy, *Biophys. J. 50*, 583−599.
45. Powers, E. T., and Powers, D. L. (2006) The kinetics of nucleated polymerizations at high concentrations: amyloid fibril formation near and above the "supercritical concentration", *Biophys. J. 91*, 122−132.
46. Lomakin, A., Teplow, D. B., Kirschner, D. A., and Benedek, G. B. (1997) Kinetic theory of fibrillogenesis of amyloid beta-protein, *Proc. Natl. Acad. Sci. U.S.A. 94*, 7942−7947.

47. Finke, J. M., Roy, M., Zimm, B. H., and Jennings, P. A. (2000) Aggregation events occur prior to stable intermediate formation during refolding of interleukin 1b, *Biochemistry 39*, 575−583.
48. Broering, J. M., and Bommarius, A. S. (2005) Evaluation of Hofmeister effects on the kinetic stability of proteins, *J. Phys. Chem. B 109*, 20612−20619.
49. Buswell, A. M., and Middelberg, A. P. (2003) A new kinetic scheme for lysozyme refolding and aggregation, *Biotechnol. Bioeng. 83*, 567−577.
50. Wiseman, R. L., Powers, E. T., and Kelly, J. W. (2005) Partitioning conformational intermediates between competing refolding and aggregation pathways: Insights into transthyretin amyloid disease, *Biochemistry 44*, 16612−16623.
51. Lepock, J. R., Ritchie, K. P., Kolios, M. C., Rodahl, A. M., Heinz, K. A., and Kruuv, J. (1992) Influence of transition rates and scan rate on kinetic simulations of differential scanning calorimetry profiles of reversible and irreversible protein denaturation, *Biochemistry 31*, 12706−12.
52. Hurshman, A. R., White, J. T., Powers, E. T., and Kelly, J. W. (2004) Transthyretin aggregation under partially denaturing conditions is a downhill polymerization, *Biochemistry 43*, 7365−7381.
53. Kueltzo, L. A., and M. C. R. (2003) Structural characterization of bovine granulocyte colony stimulating factor: Effect of temperature and pH, *J. Pharm. Sci. 92*, 1793−1804.
54. Tobler, S. A., and Fernandez, E. J. (2002) Structural features of interferon-gamma aggregation revealed by hydrogen exchange, *Protein Sci. 11*, 1340−1352.
55. Ferrone, F. A. (1985) Kinetics of sickle hemoglobin polymerization I. Studies using temperature-jump and laser photolysis techniquies, *J. Mol. Biol. 183*, 591−610.
56. Ferrone, F. A. (1985) Kinetics of sickle hemoglobin polymerization II. A double nucleation mechanism, *J. Mol. Biol. 183*, 611−631.
57. Hagen, R., Behrends, R., and Kaatze, U. (2004) Acoustical properties of aqueous solutions of urea: reference data for the ultrasonic spectrometry of liquids, *J. Chem. Eng. Data 49*, 988−991.
58. Privalov, P. L. (1979) Stability of proteins, *Adv. Protein Chem. 33*, 167−241.
59. Gekko, K., and Noguchi, H. (1979) Compressibility of globular-proteins in water at 25 °C, *J. Phys. Chem. 83*, 2706−2714.
60. Privalov, P. L., and Potekhin, S. A. (1986) Scanning microcalorimetry in studying temperature-induced changes in proteins, *Methods Enzymol. 131*, 4−51.
61. Becktel, W., and Schellman, J. (1987) Protein stability curves, *Biopolymers 26*, 1859−1877.
62. Silva, J. L., Miles, E. W., and Weber, G. (1986) Pressure dissociation and conformational drift of the beta dimer of tryptophan synthase, *Biochemistry 25*, 5780−5786.
63. Pace, C. N., Shirely, B. A., and Thomson, J. A. (1989) Measuring the Conformational Stability of a Protein, in *Protein Structure, a Practical Approach* (Creighton, T. E., Ed.) pp 311−330, IRL Press at Oxford University Press, New York.
64. Otzen, D. E., Kristensen, O., Proctor, M., and Oliveberg, M. (1999) Structural changes in the transition state of protein folding: alternative interpretations of curved chevron plots, *Biochemistry 38*, 6499−6511.
65. Hiemenz, P. C., and Rajagopalan, R. (1997) *Principles of Colloid and Surface Chemistry*, 3rd ed., Marcel Dekker, New York.
66. Freifelder, D. (1999) *Physical Biochemistry. Application to Biochemistry and Molecular Biology*, 2nd ed., W. H. Freeman and Company, New York.
67. Schmid, F. X. (1989) Spectral Methods of Characterizing Protein Conformation and Conformational Changes, in *Protein Structure. A Practical Approach* (Creighton, T. E., Ed.) pp 251−286, IRL Press at Oxford University Press, New York.
68. Finkelstein, A. V. (2003) Proteins: structural, thermodynamic and kinetic aspects, *Slow Relaxations and Nonequilibrium Dynamics in Condensed Matter*, NATO Advanced Study Institute Euro Summer School Ecole Thematique du CNRS, 77th, Les Houches, France, July 1−26, 2002, pp 649−703.
69. Oliveberg, M., and Wolynes, P. G. (2005) The experimental survey of protein-folding energy landscapes, *Q. Rev. Biophys. 38*, 245−288.
70. Shiao, D. F., Lumry, R., and Fahey, J. (1971) Studies of chymotrypsinogen family of proteins. 11. Heat-capacity changes accompanying reversible thermal unfolding of proteins, *J. Am. Chem. Soc. 93*, 2024−2035.
71. Plotnikov, V. V., Brandts, J. M., Lin, L. N., and Brandts, J. F. (1997) A new ultrasensitive scanning calorimeter, *Anal. Biochem. 250*, 237−244.
72. Jackson, W. M., and Brandts, J. F. (1970) Thermodynamics of protein denaturation: a calorimetric study of reversible denaturation of chymotrypsinogen and conclusions regarding accuracy of 2-state approximation, *Biochemistry 9*, 2294−2301.
73. Clark, P. L., Weston, B. F., and Gierasch, L. M. (1998) Probing the folding pathway of a B-Clam protein with single-tryptophan constructs, *Folding Des. 3*, 401−412.
74. Poklar, N., Vesnaver, G., and Lapanje, S. (1994) Denaturation behavior of alpha-chymotrypsinogen-A in urea and alkylurea solutions - fluorescence studies, *J. Protein Chem. 13*, 323−331.
75. Pjura, P. E., Lenhoff, A. M., Leonard, S. A., and Gittis, A. G. (2000) Protein crystallization by design: chymotrypsinogen without precipitants, *J. Mol. Biol. 300*, 235−9.
76. Oliveberg, M., Tan, Y. J., Silow, M., and Fersht, A. R. (1998) The changing nature of the protein folding transition state: implications for the shape of the free-energy profile for folding, *J. Mol. Biol. 277*, 933−43.
77. Oliveberg, M., Tan, Y. J., and Fersht, A. R. (1995) Negative activation enthalpies in the kinetics of protein folding, *Proc. Natl. Acad. Sci. U.S.A. 92*, 8926−8929.

BI700296F